Eur. Phys. J. C (2025) 85:1081
https://doi.org/10.1140/epjc/s10052-025-14780-z

THE EUROPEAN PHYSICAL JOURNAL C

Regular Article - Theoretical Physics

Black hole surrounded by perfect fluid dark matter in STV gravity: particle dynamics, thermodynamics, gravitational weak lensing and EHT tests

Sirojiddin Saydullayev[1,a], **Isomiddin Nishonov**[2,3,b], **Muysin Dusaliyev**[4,c], **Obid Xoldorov**[3,d], **Sardor Murodov**[5,6,e], **Shavkat Karshiboev**[7,f], **Sunnatillo Urinov**[8,g], **Bekzod Rahmatov**[9,10,11,h]

[1] Alfraganus University, Yukori Karakamish Street 2a, 100190 Tashkent, Uzbekistan
[2] Physics and Chemistry Department, National Research University TIIAME, Kori Niyoziy 39, 100000 Tashkent, Uzbekistan
[3] Samarkand State University, University Avenue 15, 140104 Samarkand, Uzbekistan
[4] Shahrisabz State Pedagogical Institute, Shahrisabz Str. 10, 181301 Shahrisabz, Uzbekistan
[5] New Uzbekistan University, Movarounnahr Street 1, 100007 Tashkent, Uzbekistan
[6] Institute of Fundamental and Applied Research, Kori Niyoziy 39A, 100000 Tashkent, Uzbekistan
[7] Samarqand State Pedagogical Institute, Spitamen Shokh Street 166, 140100 Samarkand, Uzbekistan
[8] Ulugh Beg Astronomical Institute, Astronomy Str. 33, 100052 Tashkent, Uzbekistan
[9] Tashkent International University of Education, Imom Bukhoriy 6, 100207 Tashkent, Uzbekistan
[10] University of Tashkent for Applied Sciences, Str. Gavhar 1, 100149 Tashkent, Uzbekistan
[11] Tashkent State Technical University, 100095 Tashkent, Uzbekistan

Received: 24 July 2025 / Accepted: 11 September 2025

Abstract In this work, we explore the physical and observational properties of a static, spherically symmetric black hole solution in scalar–tensor–vector gravity (STVG), also known as modified gravity (MOG), in the presence of perfect fluid dark matter (PFDM). We analyze the motion of magnetized and neutral particles, focusing on the effective potential, innermost stable circular orbits (ISCO), and energy extraction efficiency via the Novikov–Thorne accretion model. Our results show that the MOG parameter α and the PFDM parameter λ significantly influence the particle dynamics, stability conditions, and the efficiency of energy extraction. We also investigate thermodynamic quantities such as Hawking temperature, entropy, heat capacity, and Gibbs free energy, and find that PFDM and MOG parameters critically affect the black hole's thermal stability and phase transitions. Additionally, we study gravitational lensing in uniform and non-uniform plasma environments and compute light deflection angles modified by both MOG and PFDM effects. Finally, we analyze the shadow cast by the black hole and compare it with Event Horizon Telescope (EHT) observations of M87* and Sgr A*, providing constraints on the MOG and PFDM parameters. Our results suggest that while general relativity remains a good approximation, small deviations due to modified gravity and surrounding dark matter effects cannot be ruled out.

1 Introduction

Black holes (BHs) represent one of the most compelling and extreme manifestations of gravity in the universe. These objects, predicted by the theory of general relativity (GR), are not merely endpoints of stellar evolution but have emerged as crucial laboratories for exploring the intersection of gravitation, high-energy physics, quantum theory, and cosmology. Their event horizons, where the escape velocity equals the speed of light, render them unique testbeds for probing the nature of spacetime and the fundamental forces of nature [1,2].

Despite the remarkable empirical successes of GR, especially in weak-field regimes and through observations such as the precession of Mercury's orbit, gravitational wave detection, and the recent imaging of black hole shadows, the theory

[a] e-mail: sirojiddin.asatullayevich@mail.ru
[b] e-mail: isomiddinniwonov96@gmail.com (corresponding author)
[c] e-mail: muysin454@gmail.com
[d] e-mail: obidxoldorov@gmail.com
[e] e-mail: mursardor@ifar.uz
[f] e-mail: shavkat.qarshiboyev.89@bk.ru
[g] e-mail: mansanovich@mail.ru
[h] e-mail: rahmatovbekzod@samdu.uz

Published online: 30 September 2025

remains incomplete [3,4]. Specifically, GR encounters significant challenges when confronted with the cosmological phenomena of dark matter and dark energy, which together account for approximately 95% of the total energy content of the universe. Moreover, the theory predicts singularities—regions where curvature becomes infinite and physical laws break down, signaling the need for a more comprehensive gravitational framework [5].

In response to these conceptual and observational limitations, numerous extensions and alternatives to GR have been proposed. Among them, scalar–tensor–vector gravity (STVG), also referred to as modified gravity (MOG) [6,7], has garnered growing interest. STVG modifies the Einstein–Hilbert action by incorporating a scalar field that modulates the gravitational constant and introduces a massive vector field that mediates an additional repulsive force. This framework has demonstrated promising results in explaining galaxy rotation curves, cluster dynamics, and gravitational lensing phenomena without invoking non-baryonic dark matter [8,9].

Parallel to developments in modified gravity theories, there has been increasing focus on modeling dark matter not as a collisionless set of particles but rather as a continuous fluid with thermodynamic properties. The perfect fluid dark matter (PFDM) model represents one such approach, treating dark matter as a barotropic fluid characterized by pressure and density distributions. When incorporated into the gravitational field of a black hole, PFDM modifies the surrounding spacetime, yielding a rich array of dynamic and thermodynamic effects [10]. These effects are especially pronounced in the behavior of test particles, the structure of accretion disks, and the thermal stability of the black hole.

This paper aims to explore in detail the physical and observational implications of a static, spherically symmetric black hole solution within the STVG framework in the presence of PFDM [11,12]. The motivation lies in understanding how the interplay between modified gravity and fluidic dark matter can influence astrophysical observables, potentially offering alternative explanations to phenomena traditionally attributed to invisible matter components.

We commence by analyzing the geodesic motion of neutral and charged particles around the black hole, placing special emphasis on the modifications induced by the MOG parameter α and the PFDM parameter λ [13,14]. Such analysis sheds light on the nature of stable orbits, energy conditions, and the potential detectability of MOG-induced deviations from GR predictions in high-energy astrophysical systems.

Subsequently, the thermodynamic behavior of the black hole is scrutinized by computing key quantities such as the Hawking temperature, Bekenstein–Hawking entropy, and specific heat capacity. These quantities allow us to investigate the possibility of phase transitions and stability thresholds in the black hole's thermal evolution, potentially unveiling signatures of new physics in the strong-field regime [15].

A further component of our study involves gravitational lensing, a phenomenon where light rays are bent due to spacetime curvature. In particular, we consider weak lensing scenarios under both uniform and non-uniform plasma media. The inclusion of plasma effects is essential for modeling realistic astrophysical environments where electromagnetic waves propagate through ionized media. By deriving the deflection angles and time delays for photon trajectories, we highlight how PFDM and MOG can lead to measurable deviations from standard lensing profiles [16].

In addition, we explore the black hole shadow—a dark region bounded by a bright photon ring—as a powerful observable accessible to very-long-baseline interferometry (VLBI) observations. Using our extended gravitational model, we simulate shadow geometries and compare them against empirical data obtained by the Event Horizon Telescope (EHT) for supermassive black holes such as M87* and Sagittarius A* [17,18]. The size and shape of the shadow are shown to strongly depend on both MOG and PFDM parameters, allowing us to place bounds on their admissible ranges.

Through this integrated analysis—spanning particle dynamics, thermodynamics, lensing, and imaging—we aim to bridge theoretical developments in alternative gravity and dark matter models with cutting-edge observational astrophysics. The implications are manifold: by aligning theoretical predictions with current and future astronomical data, we can test the viability of MOG as a replacement or supplement to dark matter, refine constraints on fundamental constants, and contribute to a more unified description of gravity that remains robust in both infrared and ultraviolet regimes [19,20].

In summary, this study seeks to deepen our understanding of black holes in extended gravitational theories and fluidic dark matter scenarios, offering a holistic framework that connects theoretical insights with empirical frontiers. By doing so, it contributes to the broader pursuit of resolving some of the most profound mysteries in modern cosmology and theoretical physics [21]. In this paper, we use a geometrized system of units where $G = c = 1$, employ the sign convention $(-+++)$, and designate differentiations about the radial coordinate using primes.

2 Black holes surrounded by PFDM in STVG

Here, we explicitly study a black hole immersed in the background of PFDM in STVG. The action and the corresponding equation of motion have the form

$$S = \frac{1}{16\pi}\int d^4x\sqrt{-g}\Big(R - \frac{1}{4}B^{\mu\nu}B_{\mu\nu} + \mathcal{L}_{\rm DM}\Big), \tag{1}$$

$$R_{\mu\nu} - \frac{1}{2} g_{\mu\nu} R = T^{\phi}_{\mu\nu} - T^{\rm DM}_{\mu\nu}. \tag{2}$$

Here, $R = g^{\mu\nu} R_{\mu\nu}$ is the Ricci scalar, $g \equiv \det(g_{\mu\nu})$ is the determinant of the metric tensor, and $R_{\mu\nu}$ is the Ricci tensor. $B_{\mu\nu}$ is the massless (spin-one graviton) vector field strength tensor related to vector potential ϕ_μ, $B_{\mu\nu} = \partial_\mu \phi_\nu - \partial_\nu \phi_\mu$. In addition, $\mathcal{L}_{\rm DM}$ gives the Lagrangian density of the PFDM. $T^{\phi}_{\mu\nu}$ and $T^{\rm DM}_{\mu\nu}$ give the energy–momentum tensor for the vector field and DM, respectively.

One may assume that the vector field is an analog of the electromagnetic field, and its field tensor is defined as

$$T^{\phi}_{\mu\nu} = -\frac{1}{4\pi}\left(B^{\alpha}_{\mu} B_{\nu\alpha} - \frac{1}{4} g_{\mu\nu} B^{\alpha\beta} B_{\alpha\beta} \right), \tag{3}$$

where

$$\Delta_\mu B^{\mu\nu} = 0, \tag{4}$$

$$\Delta_\alpha B^{\mu\nu} + \Delta_\nu B^{\mu\alpha} + \Delta_\mu B^{\alpha\nu} = 0. \tag{5}$$

The energy–momentum tensors take the form

$$\left(T^{\mu}_{\nu}\right)^{\phi} = \frac{Q_g^2}{8\pi r^4} \mathrm{diag}\,(-1, -1, 1, 1)\,, \tag{6}$$

$$\left(T^{\mu}_{\nu}\right)^{\rm PFDM} = \mathrm{diag}\Big(-\rho, P_r, P_\theta, P_\phi \Big), \tag{7}$$

where $P_r = -\rho$, $P_\theta = P_\phi = P$ [22]. The equation of state for PFDM takes the form $P = \frac{1}{2}\rho$ and $\rho = -\frac{\lambda}{8\pi r^3}$, where the parameter λ stands for PFDM contributions. The gravitational source charge for the spin-one gravitational vector field ϕ_μ is $Q_g = \sqrt{\alpha} M$, where α is the field parameter that is responsible for running the gravitational constant $G = (1+\alpha) G_N$ [23].

We need to solve the gravitational field equations to obtain the desired metric. The first step is to assume a spherical symmetric ansatz for the metric in the form

$$\mathrm{d}s^2 = -e^{\chi}\mathrm{d}t^2 + e^{-\chi}\mathrm{d}r^2 + r^2(\mathrm{d}\theta^2 + \sin^2\theta \mathrm{d}\phi^2). \tag{8}$$

Here, χ is assumed to be functions of r only. Using the ansatz metric, the Einstein equations take the form [22,24]

$$e^{\chi}\left(\frac{1}{r^2} + \frac{\chi'}{r}\right) - \frac{1}{r^2} = -8\pi(1+\alpha)\rho - \frac{\alpha(1+\alpha)M^2}{r^4}, \tag{9}$$

$$\frac{e^{\chi}}{2}\left(\chi'' + (\chi')^2 + \frac{2\chi'}{r}\right) = 8\pi(1+\alpha)P + \frac{\alpha(1+\alpha)M^2}{r^4}. \tag{10}$$

Here, prime ($'$) and double prime ($''$) denote the first and second derivatives for r, respectively.

To obtain a second-order differential equation, we use the sum of equations (9)+(10), assuming $\chi = \ln f(r)$, and we have

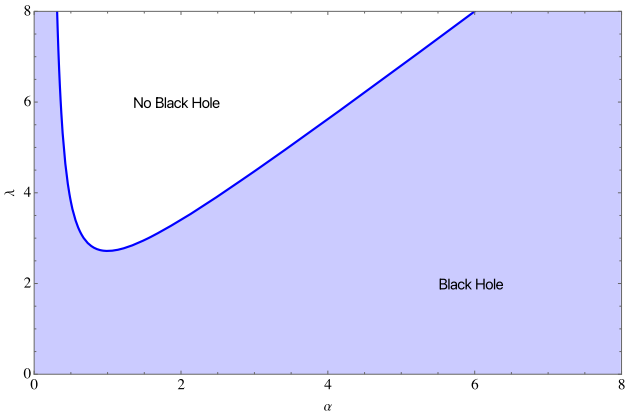

Fig. 1 Plots of the region where a black hole can exist or not

$$r^2 f''(r) + 3r f'(r) + f(r) - \frac{\alpha(1+\alpha)M^2}{r^2} = 1. \tag{11}$$

The solution of the differential equation (11) is

$$f(r) = 1 + \frac{c_1}{r} + \frac{\alpha M^2}{r^2} + \frac{c_2}{r}\ln r, \tag{12}$$

using the constants $c_1 = -2M - \lambda \ln|\lambda|$ and $c_2 = \lambda$ to satisfy the solution MOG and GR limits. Thus, we have a Schwarzschild MOG black hole solution as

$$f(r) = 1 - \frac{2(1+\alpha)M}{r} + \frac{\alpha(1+\alpha)M^2}{r^2} + \frac{\lambda}{r}\ln\frac{r}{|\lambda|}. \tag{13}$$

In the above expression (13), M represents the mass of the black hole, and α is the MOG parameter.

In Fig. 1 we show the possible region by the shaded area for the existence of a black hole/no black hole in the λ–α plane. We note that the PFDM and the MOG parameters result in a greater area for its existence.

3 Neutral particle motion

Neutral particle motion refers to the movement of particles that possess no net electric charge. Electric fields do not influence these particles due to their lack of charge. However, they may still be subject to other forces, such as gravitational, magnetic, or particle interactions. Examples of neutral particles include neutrons, neutrinos, and certain atoms or molecules with equal protons and electrons. Understanding the motion of neutral particles is crucial in various scientific fields, including nuclear physics, astrophysics, and materials science. Studying how neutral particles move and interact with their surroundings provides insights into the behavior of matter under different conditions and aids in understanding fundamental processes in the universe.

The Hamilton–Jacobi equation, which takes into account the interactions between the magnetized particles and both scalar and magnetic fields, has the form

$$g^{\mu\nu}\left(\frac{\partial S}{\partial x^{\mu}}-q\Phi_{\mu}\right)\left(\frac{\partial S}{\partial x^{\nu}}-q\Phi_{\nu}\right)=-m^{2}, \tag{14}$$

where $q=\sqrt{\alpha}m$ is the gravitational test particle charge, and $q\Phi_{\mu}$ is the term that defines the MOG interaction between the particles and the scalar field. There is an additional interaction between the particles and the scalar field,

$$\Phi_{\mu}=\frac{\sqrt{\alpha}M}{r}\left(-1,0,0,0\right). \tag{15}$$

The Lagrangian of the magnetized particles near the PFDM black holes in MOG has a form that includes the MOG interaction,

$$\mathcal{L}=\frac{1}{2}mg_{\mu\nu}u^{\mu}u^{\nu}+q\Phi_{\mu}u^{\mu}\,. \tag{16}$$

Using the above Lagrangian, one can easily find the integrals of motion of magnetized particles ($p_{\phi}=L=mu^{\phi}$ and $p_{t}=-E=mu^{t}$ denoting the total angular momentum and total energy of the particle, respectively) in the following form:

$$-\mathcal{E}=g_{tt}\dot{t}+\frac{q}{m}\Phi_{t}, \tag{17}$$

$$l=g_{\phi\phi}\dot{\phi}, \tag{18}$$

where $\mathcal{E}=E/m$ and $l=L/m$ are the specific energy and angular momentum, respectively. In solving the above Eqs. (17) and (18), we obtain

$$\dot{t}=\frac{\mathcal{E}+\frac{q}{m}\Phi_{t}}{-g_{tt}}, \tag{19}$$

$$\dot{\phi}=\frac{l}{g_{\phi\phi}}. \tag{20}$$

The Hamilton–Jacobi action for the motion of magnetized particles in the equatorial plane ($\theta=\pi/2$) can be separated as follows:

$$S=-Et+L\phi+S_{r}(r). \tag{21}$$

By making use of the Hamilton–Jacobi equation (14), we can easily obtain the equation of radial motion of the magnetized particles:

$$\begin{aligned}g_{rr}\dot{r}^{2}&=-\left[g^{tt}\left(\mathcal{E}+\frac{q\Phi_{t}}{m}\right)^{2}+g^{\phi\phi}l^{2}+1\right]\\&=\left[\mathcal{E}-V_{\text{eff}}^{+}(r)\right]\left[\mathcal{E}-V_{\text{eff}}^{-}(r)\right].\end{aligned} \tag{22}$$

After certain calculations, we obtain the effective potential in the following form:

$$V_{\text{eff}}^{\pm}=\frac{\alpha M}{r}\pm\sqrt{-g_{tt}\left(1+g^{\phi\phi}l^{2}\right)}\,. \tag{23}$$

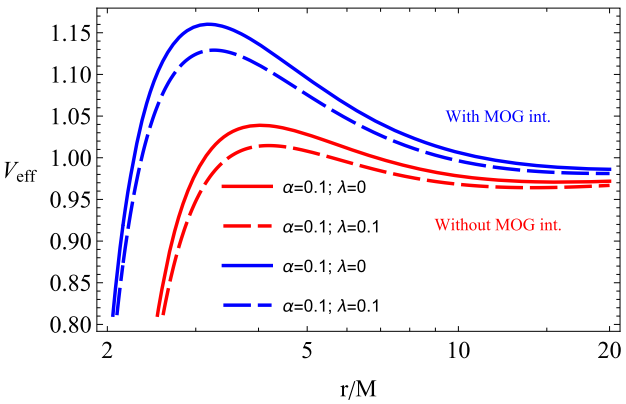

Fig. 2 Radial dependence of the effective potential at various discrete values of the parameters λ and α

In case we do not consider the MOG interaction, the effective potential takes the value

$$V_{\text{eff}}=-g_{tt}\left(1+g^{\phi\phi}l^{2}\right). \tag{24}$$

Figure 2 shows the radial behavior of the effective potential in the presence and absence of the MOG interaction, in red and blue curves, respectively. It is observed that the MOG interaction and the parameter α reduce the instability and increase the stability along r. Furthermore, the MOG interaction further enhances the stability of orbits, resulting in more stable orbits than Schwarzschild black holes and black holes without the MOG interaction. It is also worth noting that, compared to other cases, the Schwarzschild black hole exhibits the most unstable orbits. The length parameter a does not change the maximum effective potential but shifts it toward the black hole.

3.1 Circular motion

We explain the circular motion of particles around regular MOG black holes in PFDM. To describe the above concept, we utilize the following requirements for circular motion:

$$V_{\text{eff}}=\mathcal{E},\qquad V_{\text{eff}}^{\prime}=0. \tag{25}$$

To determine the stability of circular orbits around a compact gravitational object, one has to ensure that the effective potential is minimal at that position.

3.2 ISCO

The innermost stable circular orbit (ISCO) can be mathematically represented by the equation $\partial_{rr}V_{\text{eff}}=0$. Typically, this criterion is combined with the circularity condition given in Eq. (25), which defines the ISCO. As a result, the equation

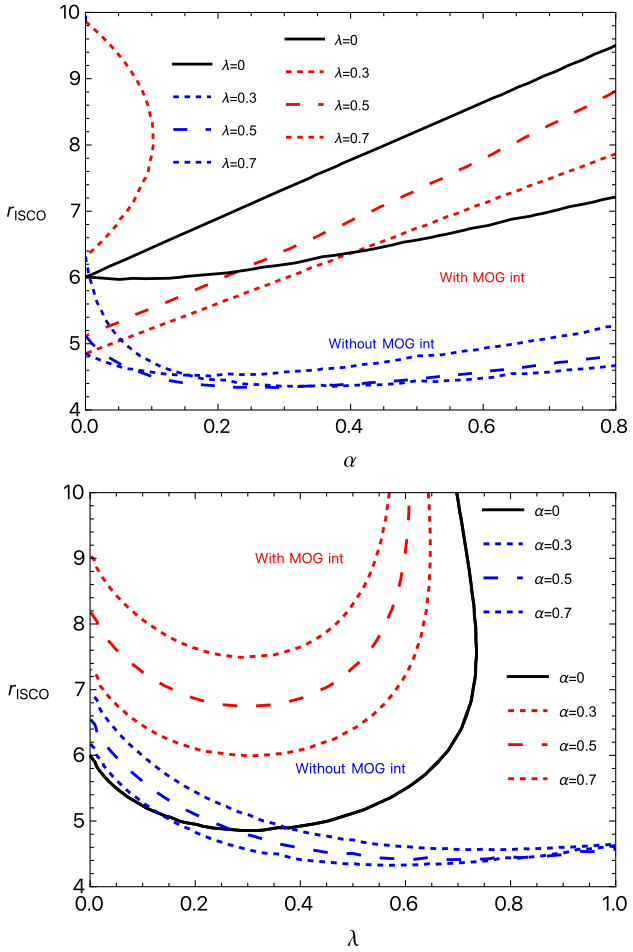

Fig. 3 Graphical representation of the ISCO radius along the dimensionless parameter α for two different values of the MOG parameter

for the effective potential provided in Eq. (23) undergoes modification to fulfill these conditions.

Figure 3 illustrates the graphical description highlighting the significant impact of both MOG interactions and the PFDM parameter on the ISCO radius. In particular, the MOG interactions amplify the increase in $r_{\rm ISCO}$ along α, and this effect becomes more intense in the absence of MOG impacts (λ). The black-bounce parameter decreases the $r_{\rm ISCO}$ in both cases, i.e., in the presence and absence of the MOG interactions. Thus, one can have higher $r_{\rm ISCO}$ values for the Schwarzschild case at $\lambda = \alpha = 0$. Furthermore, it is worth noting that the MOG interactions vanish at $\alpha = 0$, and the $r_{\rm ISCO}$ of "With MOG int" meets the $r_{\rm ISCO}$ of the "Without MOG int" case. It is also observed that MOG interaction weakens the MOG effects.

In Fig. 4, we have plotted the graphical behavior of angular momentum at the ISCO of particles in the MOG spacetime along α and $r_{\rm ISCO}$ in the left and right panels, respectively. We noted that for $\lambda = 0$, $\mathcal{L}_{\rm ISCO}$ increases along α in both cases (with and without MOG interaction). However, in the absence of MOG interactions, the increase becomes more pronounced. Hence, we can conclude that the MOG interactions diminish the angular momentum along α, and in addition, $\mathcal{L}_{\rm ISCO}$. As a result, the blue dashed curves (with MOG interaction) show higher $\mathcal{L}_{\rm ISCO}$ values than the blue curves for the same α. The angular momentum at the ISCO behaves similarly along $r_{\rm ISCO}$; it has smaller values when MOG interactions are taken into account than when they are not (for details, please see Fig. 4). Furthermore, it increases linearly for both $\lambda = 0$ and $\lambda \neq 0$ along $r_{\rm ISCO}$ for both cases (with and without MOG interactions). Notably, black holes with nonzero MOG parameters have higher $\mathcal{L}_{\rm ISCO}$ than those without PFDM effects.

The graphical illustration of Fig. 5 shows the radial dependence of energy at the ISCO along $\mathcal{L}_{\rm ISCO}$ (right panel) and $r_{\rm ISCO}$ (left). For both $\lambda = 0$ and $\lambda \neq 0$, energy at the ISCO reveals the same behavior along $\mathcal{L}_{\rm ISCO}$ and $r_{\rm ISCO}$. As in both cases, the $\mathcal{E}_{\rm ISCO}$ decreases without considering the MOG interaction while showing a much higher increase by considering the MOG interaction along $\mathcal{L}_{\rm ISCO}$. In addition, the PFDM parameter considerably contributes to the $\mathcal{E}_{\rm ISCO}$ in both cases. In contrast, its impacts on $\mathcal{E}_{\rm ISCO}$ decrease effects of the MOG interactions, particularly at higher values of $\mathcal{L}_{\rm ISCO}$. Moreover, the left panel shows how the ISCO energy changes with the parameter α under different conditions. For instance, the MOG interaction and a have influenced these relationships.

4 Energy extraction efficiency

The Novikov–Thorne accretion disc model explains Keplerian accretion around astrophysical compact gravitating objects like black holes/no black holes as a geometrically thin disk. The efficiency of the energy extraction process in the accretion disk around the gravitating objects refers to the maximum amount of energy that matter falling into the central black hole from the disk extracts as radiation energy. The efficiency of particle accretion can be calculated as $\eta = 1 - \mathcal{E}_{\rm ISCO}$, where $\mathcal{E}_{\rm ISCO}$ is characterized by the ratio of the binding energy (black hole-particle system) and rest energy of the test particle [25].

Indeed, the bolometric luminosity of the brightness emanating from the accretion disk is directly linked to the energy efficiency of the central black hole, as expressed by the equation $\eta = L_{\rm bol}/(\dot{M}c^2)$, where $\dot{M}$ signifies the accretion rate [26]. Here, we also study the efficiency of released energy at various values of parameters α and λ. The effects of the MOG parameter on the efficiency of the accretion of test particles around regular black holes in MOG are plotted in Fig. 6 along α. Interestingly, both MOG interaction and the length parameter λ significantly impact energy efficiency. The efficiency increases gradually without considering the MOG interac-

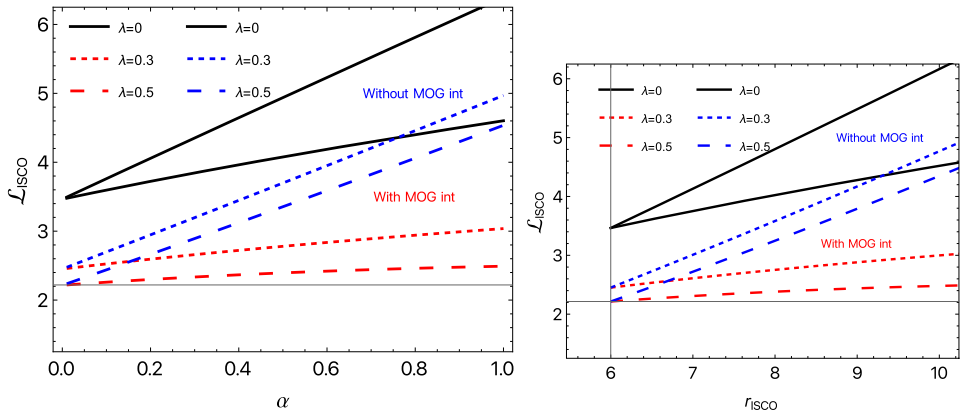

Fig. 4 Graph illustrating the behavior of angular momentum at the ISCO along α (left) and r_{ISCO} (right), both with and without considering the MOG interactions

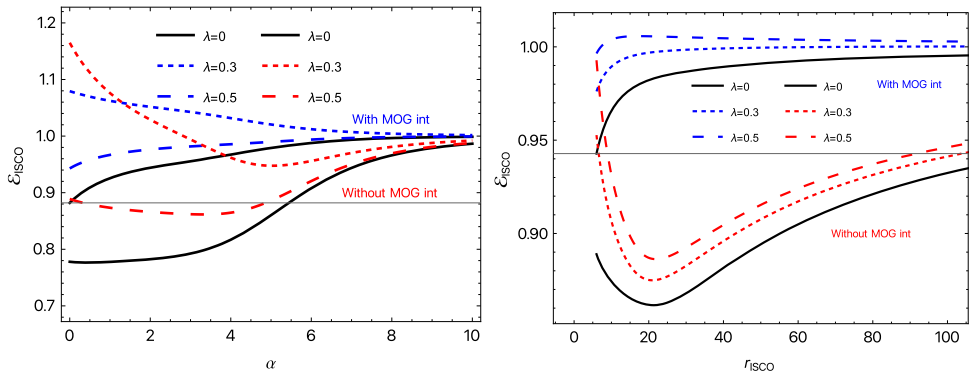

Fig. 5 Graphs showing the behavior of $\mathcal{E}_{ISCO}$ along $\mathcal{L}_{ISCO}$ (right panel) and r_{ISCO} (middle panel), and along α (left panel)

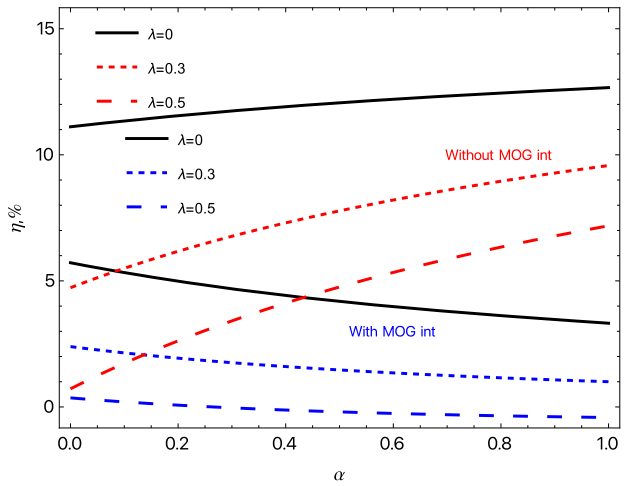

Fig. 6 Graph showing how the energy efficiency (η) changes along the parameter α under different conditions

tion, whereas it diminishes rapidly in the case of MOG interactions along α. Furthermore, the MOG parameter reduces the efficiency along α in both cases. Consequently, the efficiency reaches its maximum at $\alpha = 1$ without considering MOG interactions.

5 Thermodynamics of BHs surrounded by PFDM

To discuss the thermodynamic properties, we calculate various thermodynamic parameters in terms of r_+. The gravitational mass of a BH is determined by $f(r_+) = 0$, which gives [23]

$$M = \frac{r_+}{\alpha} - \frac{1}{\alpha}\sqrt{\frac{r_+}{(1+\alpha)}\left(r_+ - \alpha\lambda \log|\lambda|\,.\right)} \tag{26}$$

The Hawking temperature associated with the BH is given as $T = \kappa/2\pi$, where κ is the surface gravity defined by [27]

$$\kappa^2 = -\frac{1}{4} g^{tt} g^{ij} g_{tt,i} g_{tt,j}. \tag{27}$$

Using the obtained metric function, we get

$$\kappa = \left|\frac{f'(r_+)}{2}\right|. \tag{28}$$

Hence, with the help of Eq. 28 we have the surface gravity obtained as

$$\kappa = \frac{1}{2}\left[\frac{2(1+\alpha)M}{r_+^2} - \frac{2\alpha(1+\alpha)M^2}{r_+^3} - \frac{\lambda}{r_+^2}\ln\left(\frac{r_+}{\lambda}\right) + \frac{\lambda}{r_+^2}\right]. \tag{29}$$

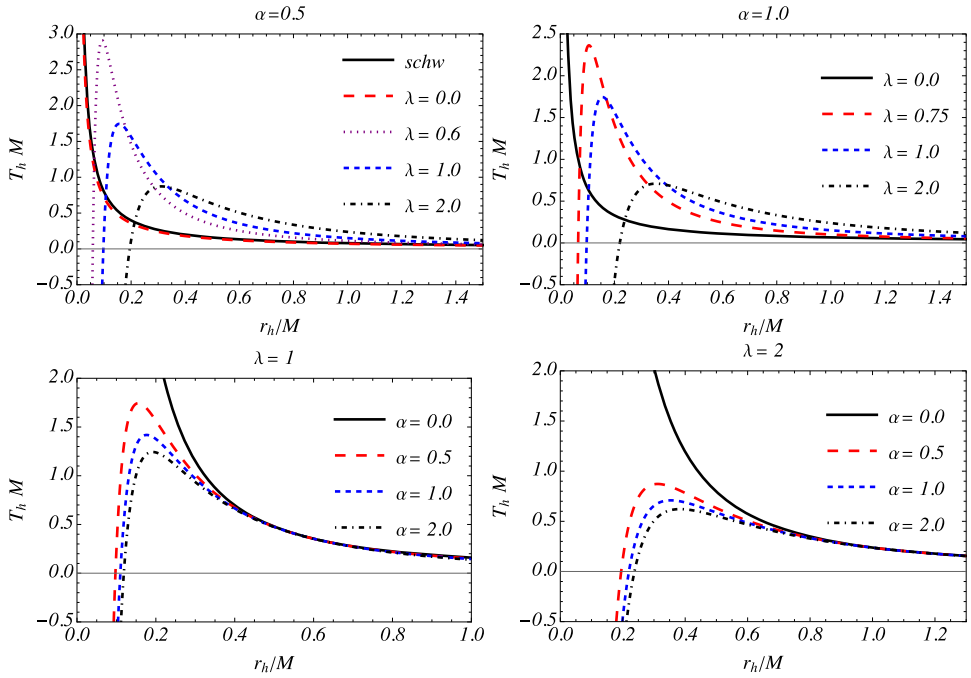

Fig. 7 The variation in temperature with r/M (top) for different values of PFDM parameter λ at $\alpha = 0.5$, 1 and (bottom) for different values of MOG α at $\lambda = 1.0, 2.0$

Substituting the value of M from Eq. (26) into the above, we obtain the expression for surface gravity

$$\kappa = -\frac{1}{\alpha r} + \frac{\lambda}{2r^2}(1 + \log\frac{r}{|\lambda|}) + \frac{1}{\alpha r^2}\sqrt{r(1+\alpha)(r + \alpha\lambda\log\frac{|\lambda|}{r})}. \tag{30}$$

Accordingly, the Hawking temperature of the BH on the outer horizon is given as [27]

$$T = \frac{\kappa}{2\pi}. \tag{31}$$

The temperature of the STVG BH surrounded by PFDM is plotted for the horizon's radius in Figs. 7 and 8. We note that in the ordinary case, at $\alpha \to 0$, as $r \to 0$, the Hawking temperature becomes infinite. This is known as the divergence or infinite-temperature problem, which implies that the BH would emit an infinite amount of radiation as it approached the Planck length. The semiclassical approximation used to derive the Hawking radiation breaks down. It suggests that a theory of quantum gravity is needed to understand the behavior of BHs at these scales. It is observed that the Hawking temperature grows first to a peak value at a critical horizon radius and then decreases to zero rapidly at a constant value of MOG and PFDM parameters. It turns out that the maximum value of the Hawking temperature increases with increasing PFDM parameters while decreasing with an increase in the MOG parameter. Moreover, the Hawking temperature shows a peak that decreases and moves to the right when the PFDM parameter λ increases.

Further, its entropy is an important and useful thermodynamic quantity associated with the BH horizon. One can calculate the area and entropy of the STVG BH surrounded by PFDM using the following general expression [27]:

$$\mathcal{A} = \int_0^{\pi} \mathrm{d}\theta \int_0^{2\pi} \sqrt{g_{\theta\theta} g_{\phi\phi}}\, \mathrm{d}\phi. \tag{32}$$

Hence,

$$\mathcal{A} = 4\pi r_+^2, \quad S = \frac{\mathcal{A}}{4} = \pi r_+^2. \tag{33}$$

The BH obeys the area law. The presence of the PFDM parameter does not affect the entropy.

Next, to discuss the thermodynamic stability of the regular BH immersed in PFDM, we compute the heat capacity of the BH. It is well known that the thermodynamic stability of the system is related to the sign of the heat capacity. If the heat capacity is positive, the BH is stable; when it is negative, it is said to be unstable. In a state of thermodynamic equilibrium, the heat capacity of the BH is defined as

$$C = \frac{\partial M}{\partial T} = \left(\frac{\partial M}{\partial r_+}\right)\left(\frac{\partial r_+}{\partial T}\right). \tag{34}$$

Now, using Eqs. (31), (29), and (26), we obtain the expression for C, but it is too long, so it is better to indicate it in a figure. It is quite clear from Eq. (34) that the heat capacity is dependent on the PFDM parameter λ.

It is very easy to infer from Fig. 8 that for some values of α and λ, C vanishes. Also, when C vanishes, there is a value of r_+ associated with it, which is often referred to as the critical radius r_+^c.

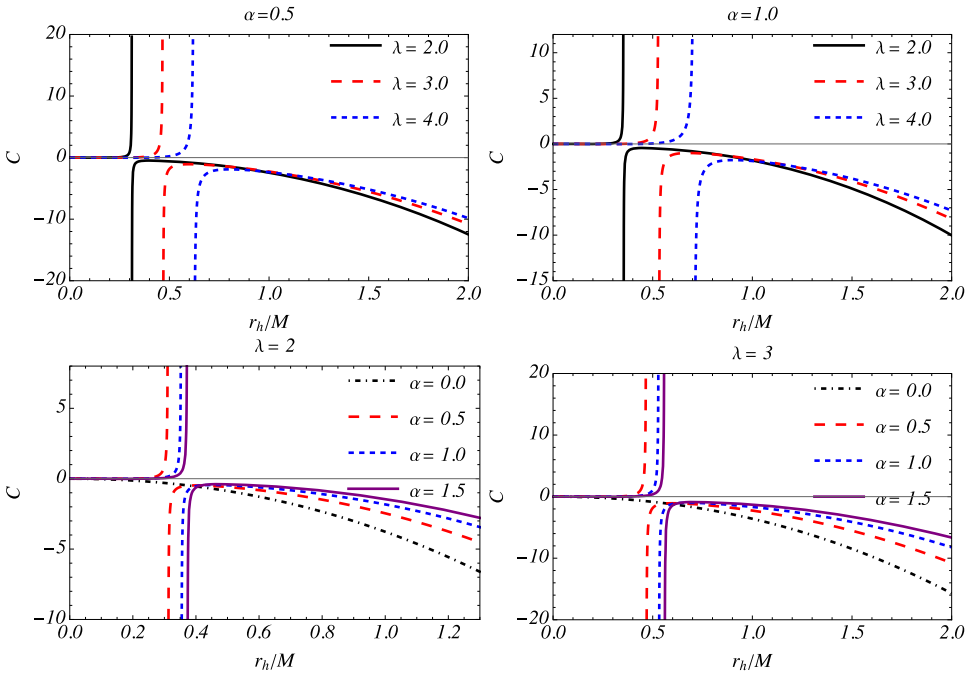

Fig. 8 Plot showing the variation in heat capacity with r (top) for different values of the PFDM parameter λ at $\alpha = 0.5, 1.0$ and (bottom) for different values of MOG α at $\lambda = 2.0, 3.0$

At this r_+^c, there is a discontinuity in heat capacity. Further, we note that the BH is thermodynamically stable, i.e. $C > 0$, when $r \in (0, r_+^c)$, and it is unstable, i.e. $C < 0$, when $r > r_+^c$. Also, when $r_+ = r_+^c$, a second-order phase transition occurs from stable to unstable, and we note both the unstable and stable states of the BH. It is worth mentioning that the critical radius r_+^c depends on the PFDM parameter. Indeed, the value of r_+^c increases with the increase in λ and MOG α in STVG. The temperature associated with this critical radius is called the critical temperature T_c.

Another important thermodynamic parameter is the Gibbs free energy, which is given as

$$G = M - TS. \tag{35}$$

Now, one of the thermodynamic quantities, the Gibbs free energy, is calculated, and its variation with BH parameters is analyzed in detail.

In Fig. 9, we plot the Gibbs free energy around a regular BH surrounded by perfect fluid dark matter. In this plot, we can see that the Helmholtz free energy has a minimum value, and thus this black hole may be thermodynamically stable.

6 Gravitational weak lensing around SV-MOG gravity surrounded by PFDM in a plasma

In this section, our main concern is to unravel the effects of gravitational lensing in the MOG black hole surrounded by a plasma, considering a weak-field approximation defined as follows [28,29]

$$g_{\alpha\beta} = \eta_{\alpha\beta} + h_{\alpha\beta}, \tag{36}$$

where $\eta_{\alpha\beta}$ and $h_{\alpha\beta}$ denote the Minkowski metric and perturbation metric, respectively, and their properties

$$\eta_{\alpha\beta} = \text{diag}(-1, 1, 1, 1), \tag{37}$$

$$h_{\alpha\beta} \ll 1, \quad h_{\alpha\beta} \to 0 \quad \text{under} \quad \mathrm{x}^{\alpha} \to \infty \tag{38}$$

$$g^{\alpha\beta} = \eta^{\alpha\beta} - h^{\alpha\beta}, \quad h^{\alpha\beta} = h_{\alpha\beta}. \tag{39}$$

We now want to study the plasma effects on the deflection angle of the light rays. For large distances, we can approximate the black hole metric as

$$ds^2 = ds_0^2 + \cdots dt^2 + \cdots dr^2, \tag{40}$$

where $\mathrm{d}s^2 = -\mathrm{d}t^2 + \mathrm{d}r^2 + r^2(\mathrm{d}\theta^2 + \sin^2\theta \mathrm{d}\phi^2)$, and R_s is the Schwarzschild radius. With the help of Eq. 36, the components $h_{\alpha\beta}$ in the Cartesian coordinates can be written as [28,30]

$$\begin{aligned} h_{00} &= \frac{(1+\alpha)R_s}{r}\left(1 - \frac{\alpha R_s}{4r}\right) - \frac{\alpha}{r}\log\frac{r}{|\lambda|}, \\ h_{ik} &= \left(\frac{(1+\alpha)R_s}{r}\left(1 - \frac{\alpha R_s}{4r}\right) - \frac{\alpha}{r}\log\frac{r}{|\lambda|}\right) n_i n_k \ , \\ h_{33} &= \left(\frac{(1+\alpha)R_s}{r}\left(1 - \frac{\alpha R_s}{4r}\right) - \frac{\alpha}{r}\log\frac{r}{|\lambda|}\right)\cos^2 x \ , \end{aligned} \tag{41}$$

where $\cos x = \frac{z}{\sqrt{b^2+z^2}}$ and $r = \sqrt{b^2+z^2}$, and b is the impact parameter signifying the closest approach of the photons to the black hole. Using the expressions mentioned above in the

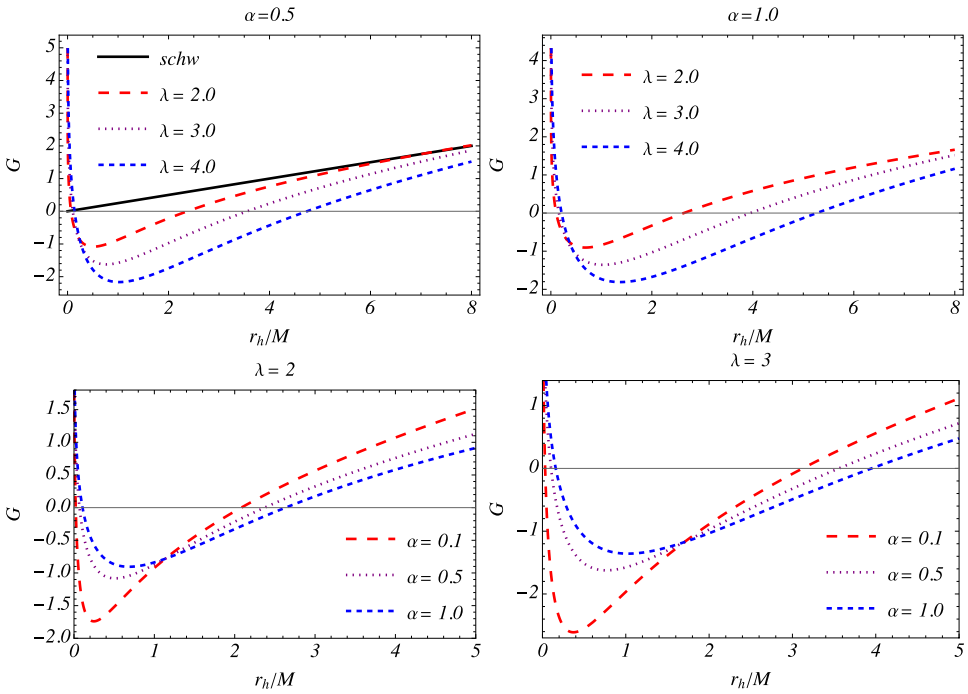

Fig. 9 Plots of G versus r (top) for different values of the PFDM parameter λ at $\alpha = 0.5$, 1.0 and (bottom) for different values of MOG α at $\lambda = 2.0$, 3.0

formula, one can compute the light deflection angle concerning b for a black hole surrounded by plasma [28,31]

$$\hat{\alpha}_i = \pm\frac{1}{2}\int_{-\infty}^{\infty}\Big[\frac{1}{2}\Big(h_{33,i} + \frac{\omega^2}{\omega^2-\omega_e^2}h_{00,i} - \frac{K_e}{\omega^2-\omega_e^2}\omega^2 N_{,i}\Big)\Big]dz. \tag{42}$$

$N(x^i)$ shows the number density of the particles in the plasma around the black hole, and $K_e = 4\pi e^2/m_e$ is a constant. The $\pm$ signs of $\hat{\alpha_i}$ determine the deflection towards and away from the central object, respectively.

Now, we can easily examine the impact of different plasma mediums on the photon deflection angle.

6.1 Uniform plasma

In this subsection, we discuss the light deflection angle around the STVG black hole surrounded by uniform plasma, which is defined as $\omega_o^2/\omega^2 = \text{const}$, using a weak gravitational lensing conception. By calculating Eq. (42), we may easily obtain an expression of the deflection angle in the following form.

$$\hat{\alpha}_{uni} = \Big(\frac{R_s}{b}(1+\alpha) + \frac{\alpha}{b}\log\frac{2|\lambda|}{b}\Big)\Big(1+\frac{1}{1-\omega_o^2/\omega^2}\Big) - \frac{\alpha}{b} - \frac{\pi R_s^2\alpha}{16b^2}(1+\alpha)\times(1+\frac{2}{1-\omega_o^2/\omega^2}). \tag{43}$$

The condition $\partial_r N = 0$ corresponds to a uniform plasma, and using Eq. (43), we may obtain a new dependence of the deflection angle of light rays on the impact parameter b, and it is presented in Fig. 10. Additionally, we can consider the influence of the MOG α and PFDM parameters on the bending angle around the BH of the photon in Fig. 11. It is evident that if the photon moves away from the black hole—namely, the impact parameter b/M is increased—the angle of deflection starts to decline. In the Fig. 10, the top and bottom panels give following result: increasing the value of α causes the bending angle to decrease, while the PFDM parameter λ is responsible for the larger one. In Fig. 11, we can see that if the bending angle is plotted as a function of the MOG parameter α, a larger value of λ causes it to increase, while smaller values have the reverse effect. In addition, if it is shown by λ's function, α causes the deflection angle to increase, except its $\alpha = 0$, because in this situation it remains unchanged.

6.2 Non-uniform plasma

Now, we calculate the deflection angle of light rays around the STVG BH with the PFDM parameter in the presence of a singular isothermal sphere (SIS) plasma medium. For the SIS, we may use the density distribution and the plasma concentration written as as [4,32]

$$\rho(r) = \frac{\sigma_v^2}{2\pi r^2}, \tag{44}$$

with σ_v^2 being a one-dimensional (1D) velocity dispersion, and

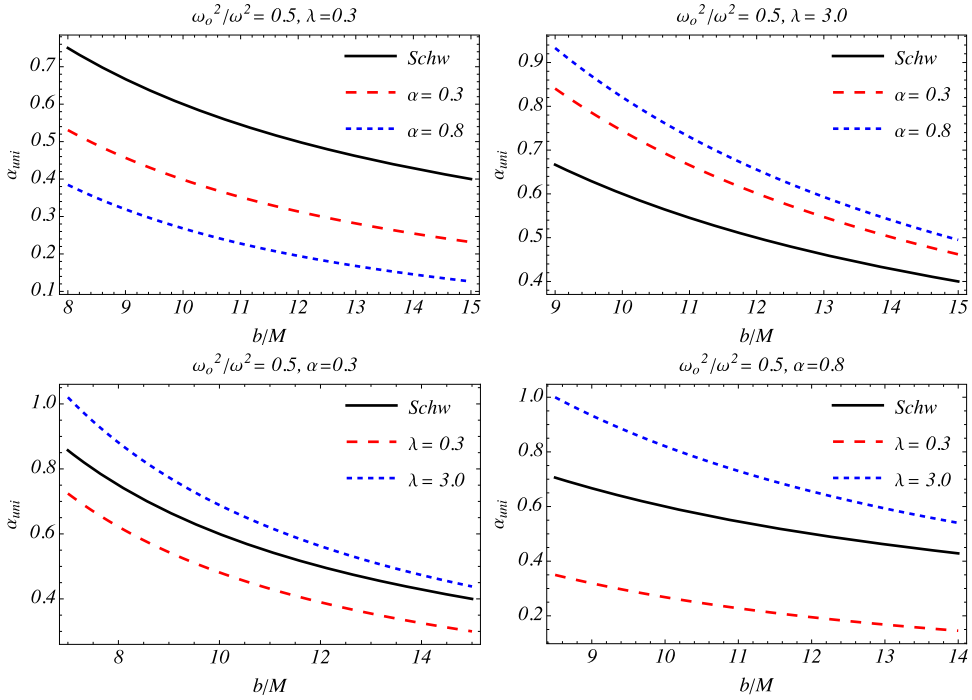

Fig. 10 Illustrations of the bending angle α_{uni} as a function of the impact parameter b/M for the PFDM parameter λ at $\alpha = 0.5, 1.0$ (top panel) and the MOG parameter α at λ =0.3 and $\lambda = 3.0$ (bottom panel) with a fixed frequency of plasma ω_0^2/ω^2

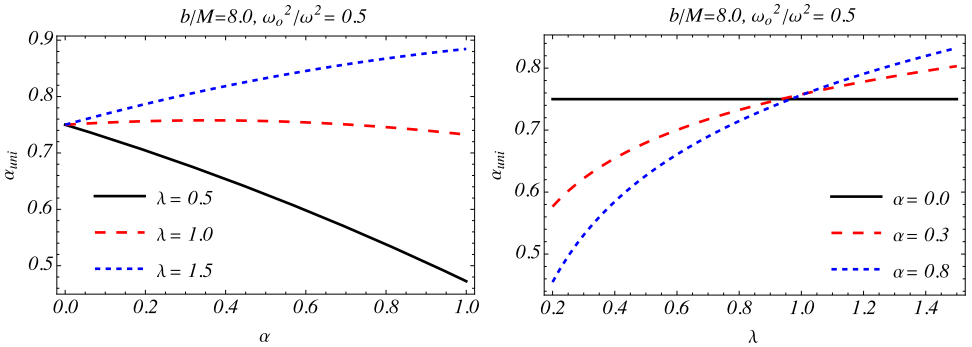

Fig. 11 Graph illustrating the behavior of the deflection angle as a function of the MOG parameter α and PFDM parameter λ

$$N(r) = \frac{\rho(r)}{\kappa m_p} \tag{45}$$

with the mass of the proton m_p and a 1D coefficient κ associated to the dark matter contribution. By using Eq. (42), the deflection angle of the light rays for the non-uniform (SIS) plasma medium can be defined as [33]

$$\hat{\alpha}_{sis} = \Big(1+\alpha\Big)\Big(\frac{2R_s}{b} + \frac{2R_s^3\omega_c^2}{3\pi b^3\omega^2} - \frac{3\pi R_s^2\alpha}{16b^2}\Big) - \frac{\alpha}{b} - \frac{R_s^2\omega_c^2}{2b^2\omega^2} + \frac{2\lambda}{b}\log[\frac{2|\lambda|}{b}]\Big(1 + \frac{R_g^2\omega_c^2}{3\pi b^2 w^2}\Big), \tag{46}$$

where ω_c^2 is used for simplicity and can be redefined in Ref. [32]. From Eq. (46), we may obtain graphs showing the dependence of the deflection angle of light rays around the BH on the impact parameter of the orbits b, which is shown in Fig. 12. In general, we have obtained similar results with uniform plasma; for large values of the impact parameter, the deflection angle goes to zero. The effect of the MOG parameter α and PFDM parameter λ with the fixed plasma parameter $\frac{\omega_e^2}{\omega^2}$ on the deflection angle of light rays can be checked with Fig. 13. It can be seen that in the left panel, λ leads to the bending of light with different quantities. For example, a large value is similarly responsible for a larger bending angle, while a smaller value corresponds to a smaller bending angle. The right panel shows how the deflection angle changes with respect to the PFDM parameter λ with various fixed MOG parameters α. We see that if α vanishes, the deflection angle is not affected by PFDM. Additionally, an increasing value of λ also causes the angle to increase.

We have further explored the bending angle with a comparison of plasma and vacuum cases. In Fig. 14, it is possible to see that the effect of uniform plasma dominates, while non-uniform plasma's impact is smaller, in contrast to the vacuum case, staying in the middle of the two of them results in $\alpha_{uni} > \alpha_{vac} > \alpha_{sis}$.

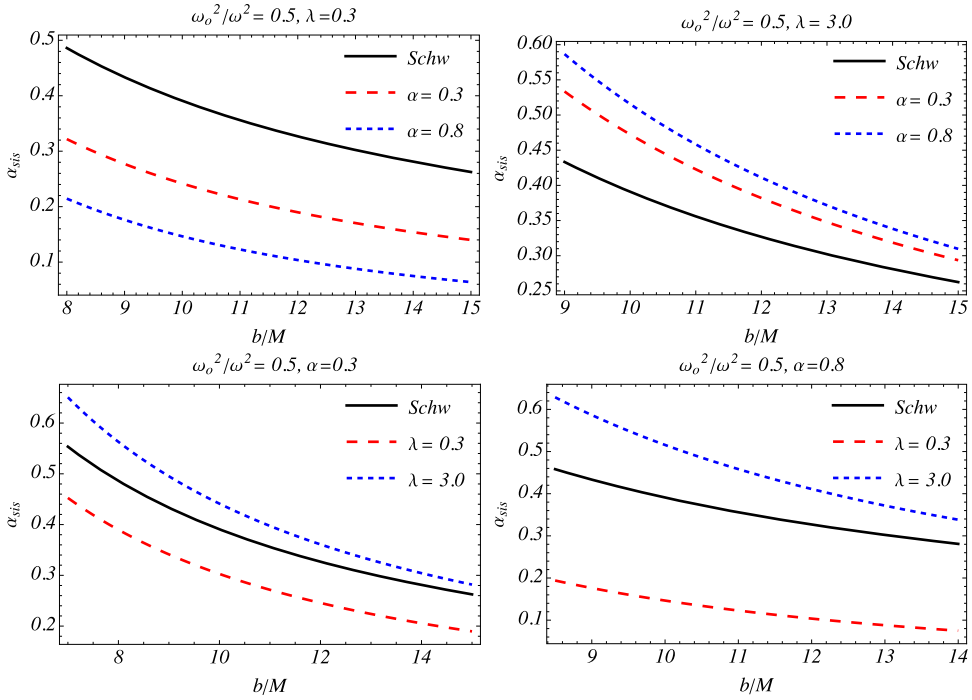

Fig. 12 Diagrams giving information about the deflection angle α_{sis} as a function of the impact parameter b/M for the PFDM parameter λ at $\alpha = 0.5, 1.0$ (top panel) and the MOG parameter α at λ =0.3 and $\lambda = 3.0$ (bottom panel), with a fixed frequency of plasma ω_0^2/ω^2

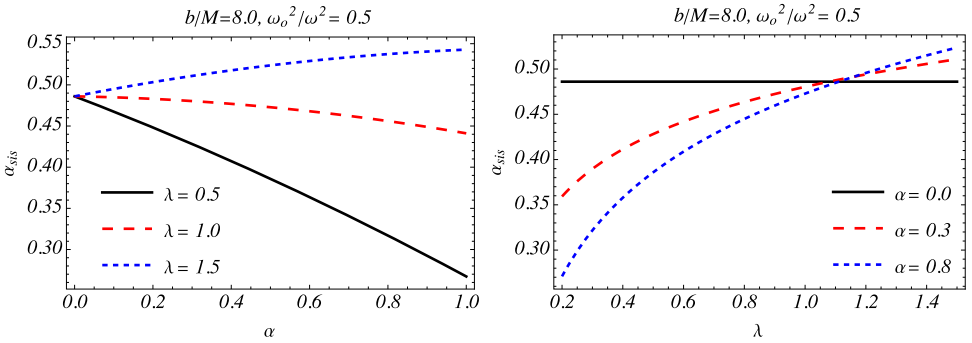

Fig. 13 Graph showing the behavior of the deflection angle with respect to the MOG parameter α and PFDM parameter λ

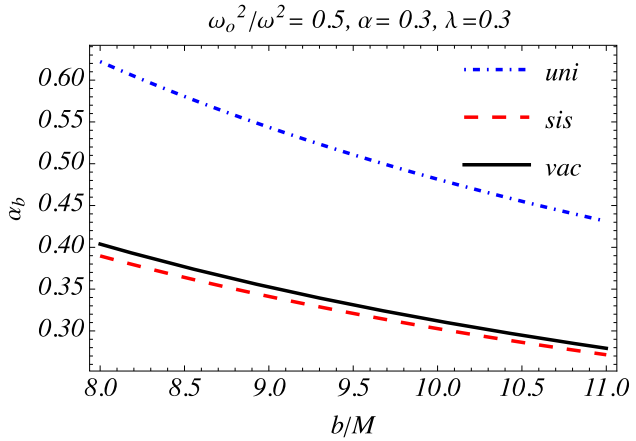

Fig. 14 Comparison of deflection angle in the case of vacuum, uniform, and SIS plasma mediums

7 Geodesic motion and the black hole's shadow

Geodesic motion around a BH is the most important aspect in predicting the potential structure of a BH shadow. Consider a test particle traveling around the BH with a rest mass of m_0. Geodesics are easier to find if the constant of motion associated with the symmetry direction is determined. Let y^σ and $v^\sigma = \mathrm{d}x^\sigma/\mathrm{d}\lambda$ be the vectors along the symmetry direction and the tangent vector along the curve $x^\sigma = x^\sigma(\tau)$, respectively, where τ is an affine parameter. Since x^μ is a geodesic [34], we may use the Killing vectors to obtain the corresponding conserved quantities along the particle's motion [35,36].

In Fig. 15, the set of plots clearly demonstrates that the size of the black hole shadow increases with both parameters α and λ. The parameter α, which may represent a modified gravity or magnetic charge term, has a more pronounced effect on the shadow radius. As α increases, the contour of the shadow expands significantly. The parameter λ, though its effect is comparatively weak, also contributes to a con-

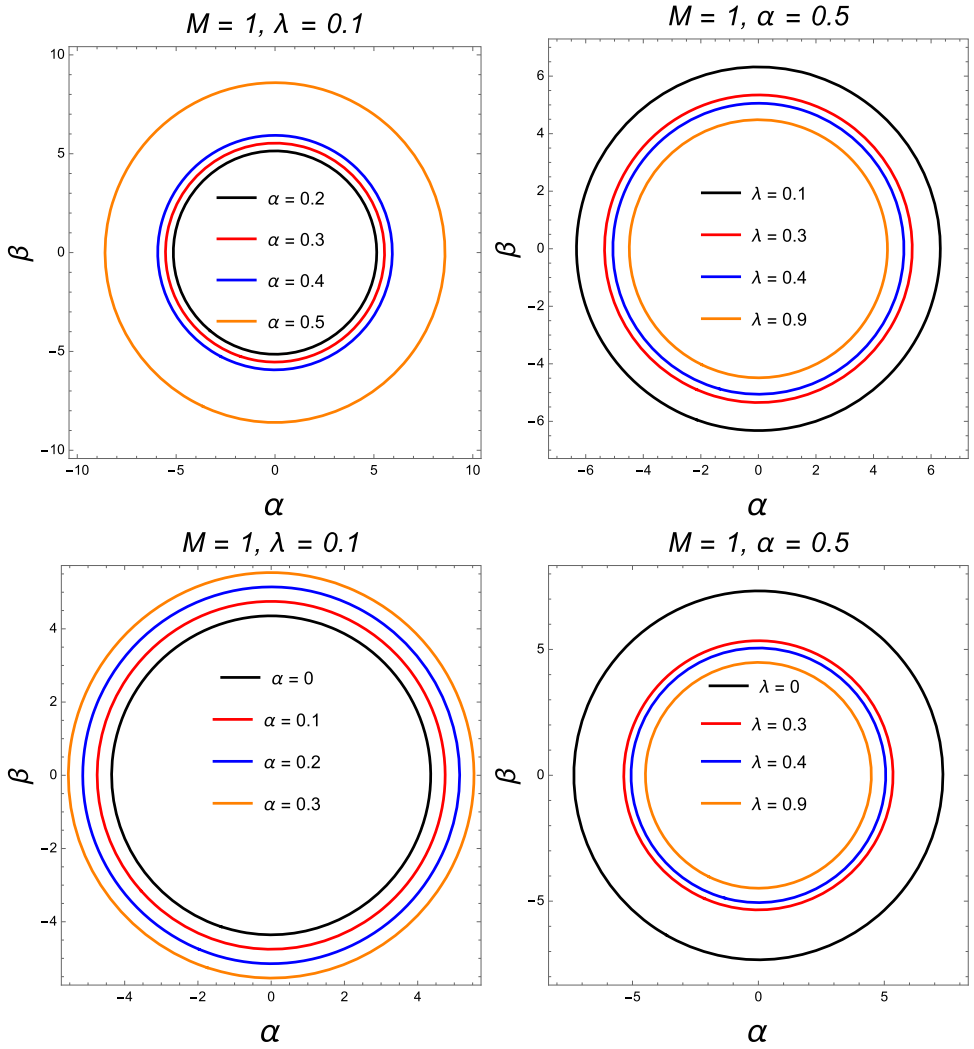

Fig. 15 Rgw radial profile of the black hole's shadow for parameter α (left panel), parameter λ (middle panel), and M (right panel) at different combinations of parameters

sistent enlargement of the shadow. This indicates that both α and λ affect the location of the photon sphere, causing it to shift outward and thus increasing the apparent size of the black hole shadow. These visual results confirm the parametric sensitivity of the black hole shadow in the considered spacetime geometry,

$$y^{\sigma} v_{\sigma} = constant. \tag{47}$$

The time-like Killing vector for a time-independent metric coefficient is provided by $y^{\sigma} = (1, 0, 0, 0)$, and the Killing vector for the ϕ direction may be expressed as $y^{\sigma} = (0, 0, 0, 1)$. By solving Eq. (47), we can establish the following relationship utilizing the equation as mentioned above:

$$y^0 v^0 = v^0 = -\mathcal{E}, \qquad y^3 v_3 = v_3 = \mathcal{L}. \tag{48}$$

$\mathcal{E}$ and $\mathcal{L}$ indicate a particle's relativistic energy and angular momentum per unit mass. The geodesic equations may now be determined using Eq. (48), as illustrated below:

$$u^0 = g^{0\mu} u_{\mu} = g^{00} u_0 = \frac{\mathcal{E}}{f(r)}, \tag{49}$$

$$u^3 = g^{3\mu} u_{\mu} = g^{33} u_3 = \frac{\mathcal{L}}{r^2 \sin^2\theta}. \tag{50}$$

This becomes

$$\frac{\mathrm{d}t}{\mathrm{d}\tau} = \frac{\mathcal{E}}{f(r)}, \qquad \frac{\mathrm{d}\phi}{\mathrm{d}\tau} = \frac{\mathcal{L}}{r^2 \sin^2\theta}. \tag{51}$$

The two remaining geodesic equations may be obtained using the Hamilton–Jacobi approach. Consequently, it may be inferred that

$$\frac{\partial S}{\partial \tau} + \frac{1}{2} g^{\mu\sigma} \frac{\partial S}{\partial x^{\mu}} \frac{\partial S}{\partial x^{\sigma}} = 0. \tag{52}$$

A proposed approach, such as the one mentioned in Ref. [34], would result in the following:

$$H = H_r - \mathcal{E}t + \mathcal{L}\phi + H_\theta + \frac{1}{2}m_0^2\tau. \tag{53}$$

In Eq. (53), H_r and H_θ represent the functions of r and θ, respectively. Introducing the Jacobi action (52) yields the Hamilton–Jacobi equation [37]

$$H_r = \int^r \frac{\sqrt{X_r}}{r^2 f(r)}\mathrm{d}r, \qquad H_\theta = \int^r \sqrt{X_\theta}\mathrm{d}\theta, \tag{54}$$

in which

$$X_r = r^4\mathcal{E}^2 - r^2\left(r^2 m_0^2 + K + \mathcal{L}^2\right) f(r), \tag{55}$$

$$X_\theta = K - \mathcal{L}^2\cot^2\theta. \tag{56}$$

The geodesic equations of motion for a particle in the presence of a non-rotating black hole may be expressed using the relation $H_\theta = \frac{\partial S}{\partial \theta} = \frac{\partial S_\theta}{\partial \theta}$ and $H_r = \frac{\partial S}{\partial r} = \frac{\partial S_r}{\partial r}$.

$$r^2\frac{\mathrm{d}\theta}{\mathrm{d}\tau} = \sqrt{K - \mathcal{L}^2\cot^2\theta}, \tag{57}$$

$$r^2\frac{dr}{\mathrm{d}\tau} = \sqrt{r^4\mathcal{E}^2 - r^2\left(r^2 m_0^2 + K + \mathcal{L}^2\right) f(r)}. \tag{58}$$

Equation (57) represents the geodesic equation along the θ direction, whereas Eq. (58) represents the geodesic equation along the r direction. Furthermore, the subsequent photon-traced geodesic equations are derived by assuming $m_0^2 = 0$ in the vicinity of the black hole [38,39].

$$r^2\frac{\mathrm{d}\theta}{\mathrm{d}\tau} = \sqrt{K - \mathcal{L}^2\cot^2\theta}, \tag{59}$$

$$r^2\frac{\mathrm{d}r}{\mathrm{d}\tau} = \sqrt{r^4\mathcal{E}^2 - r^2\left(K + \mathcal{L}^2\right) f(r)}. \tag{60}$$

On the other hand, we may write Eq. (60) as

$$\left(\frac{\mathrm{d}r}{\mathrm{d}\tau}\right)^2 + V_{\text{eff}} = 0. \tag{61}$$

The symbol V_{eff} represents the effective potential and is given by

$$V_{\text{eff}} = \frac{f(r)}{r^2}\left(K + \mathcal{L}^2\right) - \mathcal{E}^2. \tag{62}$$

The following limitations will aid in identifying the unstable circular orbits:

$$V_{\text{eff}}(r = r_p) = V_{\text{eff}}^{'}(r = r_p) = 0. \tag{63}$$

In this context, $r = r_p$ denotes the radius of a photon, and $'$ indicates the derivative concerning r. Hence, equation $V_{\text{eff}}(r_p) = 0$ indicates that

$$\frac{r_p^2}{f(r_p)} = \xi + \eta^2. \tag{64}$$

Equation (64) uses the Chandrasekhar constant definition [40], which is $\xi = K/\mathcal{E}^2$ and $\eta = \mathcal{L}/\mathcal{E}$. Similarly, $V'_{\text{eff}}(r_p) = 0$, results in

$$r_p f^{'}(r_p) - 2f(r_p) = 0. \tag{65}$$

Imagine a massless particle, like a photon, released by an object traveling toward the BH that is situated between an observer and a brilliant object. Photon paths may result in (a) scattering away, (b) falling into the BH, or (c) a critical geodesic dividing (a) and (b). The scattering of a photon from the BH is visible to the viewer during this entire process. However, a dark zone will develop when a photon enters the BH. We call this dark zone the shadow of the BH. Our primary objective in this part is to investigate the shadow emitted in PFDM spacetime by the BH. Initially, we must specify the celestial coordinates [40,41] for this purpose as

$$\alpha = \lim_{r\to\infty} -\left(r^2\sin\theta\frac{\mathrm{d}\phi}{\mathrm{d}r}\right), \tag{66}$$

$$\beta = \lim_{r\to\infty}\left(r^2\frac{\mathrm{d}\theta}{\mathrm{d}r}\right). \tag{67}$$

In this context, α represents the apparent perpendicular distance of the shadow from the axis of symmetry, whereas β represents its projection on the equatorial plane. The variable θ denotes the inclination angle between the axis of symmetry and the observer's line of sight, while r_0 indicates the distance between the black hole and the observer. The values of the derivatives $\mathrm{d}\phi/\mathrm{d}r$ and $\mathrm{d}\theta/\mathrm{d}r$ may be determined using the geodesic equations in the following manner [42,43]:

$$\frac{\mathrm{d}\phi}{\mathrm{d}r} = \frac{\mathcal{L}\csc^2\theta}{r^2\sqrt{\mathcal{E}^2 - \frac{f(r)}{r^2}\left(K + \mathcal{L}^2\right)}}, \tag{68}$$

$$\frac{\mathrm{d}\theta}{\mathrm{d}r} = \frac{1}{r^2}\sqrt{\frac{K - \mathcal{L}^2\cot^2\theta}{\mathcal{E}^2 - \frac{f(r)}{r^2}\left(K + \mathcal{L}^2\right)}}. \tag{69}$$

When Eqs. (68) and (69) are solved for $r \to \infty$, the expression for the celestial coordinates (66) assumes the following form [40,42,43]:

$$\alpha = -\eta\csc^2(\theta)\sin(\theta), \quad \beta = \pm\sqrt{\xi - \eta^2\cot^2(\theta)}. \tag{70}$$

The preceding equations are further simplified when $\theta = \pi/2$ is substituted in:

$$\alpha = -\eta, \qquad \beta = \pm\sqrt{\xi}. \tag{71}$$

As a result, the expression of the shadow radius in the celestial plane (α, β) may be computed as follows:

$$R_s^2 = \alpha^2 + \beta^2 = \eta^2 + \xi = \frac{r_p^2}{f(r_p)}. \tag{72}$$

In Eq. (72), R_s stands for the radius of the black hole's shadow when it is not revolving.

8 Constraint MOG parameters of the black hole with the EHT observations of $M87$ and $Sgr.A$

In this section, we examine the dependence of the PFDM parameters λ and α on the shadow images of the black holes M87* and Sagittarius A* (Sgr. A*) using Event Horizon Telescope (EHT) observations. Our analysis is limited to the non-rotating case, since the rotation parameter a of Sgr. A* is small enough to have a negligible effect on the shadow radius [44]. Furthermore, it is shown that it is difficult to distinguish between a Kerr black hole ($a = 0.60M$) and a non-rotating extended black hole for M87* using shadow images alone. This conclusion is supported by general/relativistic magnetohydrodynamic simulations and radiative transfer calculations that generate synthetic shadow images for direct comparison with EHT observations [45].

Furthermore, as noted in Ref. [45], the shadow size of M87* is observed to lie in the range

$$3\sqrt{3}(1 \pm 0.17)M. \tag{73}$$

Regardless of whether the underlying model assumes spherical symmetry or axisymmetry, this observation provides a strong basis for constraining theoretical models of black holes in alternative theories of general relativity and gravity. By comparing theoretical predictions of the shadow radius from our model with EHT observational data, we attempt to determine the allowable ranges for the parameters α and other relevant physical parameters. This approach allows us to probe the interplay between nonlinear electrodynamics, dark matter, and gravitational effects around black holes in the strong-field regime.

The EHT collaboration reported the following data for M87*: the angular diameter of the shadow is $\theta_{\mathrm{M87}^*} = 42 \pm 3\,\mu$as, the distance to M87* is $D = 16.8$ Mpc, and the mass of M87* is $M_{\mathrm{M87}^*} = 6.5 \pm 0.90 \times 10^9\, M_\odot$ [45]. For Sgr. A*, recent EHT results provide the angular diameter of the shadow as $\theta_{\mathrm{Sgr.A}^*} = 48.7 \pm 7\,\mu$as, the distance to Sgr. A* as $D = 8277 \pm 33$ pc, and the black hole mass as $M_{\mathrm{Sgr.\,A}^*} = 4.3 \pm 0.013 \times 10^6\, M_\odot$ (VLTI) [45]. Using the data provided, the shadow diameter in units of mass can be calculated using the following formula [38,39]:

$$d_{\mathrm{sh}} = \frac{D\theta}{M}. \tag{74}$$

The theoretical shadow diameter is given by $d_{\mathrm{sh}} = 2R_{\mathrm{sh}}$. Applying the above expression, we find the shadow diameter for M87* to be $d_{\mathrm{sh}}^{\mathrm{M87}^*} = (11 \pm 1.5)M$ [45] and for Sgr. A* to be $d_{\mathrm{sh}}^{\mathrm{Sgr.A}^*} = (9.5 \pm 1.4)M$ [44].

The relationship between α and λ affecting the black hole shadow size is shown in Fig. 16. The graphs are drawn based on EHT observational data for M87* and Sgr A*, with the α/M axis representing the charge-to-mass ratio and the d_{sh}/M axis representing the shadow diameter-to-mass ratio. The black lines correspond to $\lambda = 0$, representing the scenario where the effect of dark matter is not considered. The red dashed lines show the variation in shadow size when $\lambda = 0.03$, illustrating how the presence of dark matter influences the shadow. It can be seen that as α/M increases, the shadow diameter decreases, and this reduction occurs more rapidly when λ is present. The confidence intervals 1σ and 2σ represent the observational data provided by the EHT. When λ is absent, the black lines mostly fall within the 1σ confidence interval, indicating that the model without the influence of dark matter aligns well with the EHT observations. In contrast, the red dashed lines representing the case where λ is present mostly fall within the 2σ interval, suggesting the possible influence of dark matter. However, this influence is not as strong within the 1σ range. Thus, the graphs clearly show how the parameters α and λ affect the black hole shadow size. An increase in charge and the dark matter parameter reduces the shadow size. Based on EHT observations, the absence of λ corresponds more closely to the 1σ interval, indicating a minimal influence of dark matter. However, the presence of λ aligns with the 2σ interval, suggesting the possible existence of dark matter.

9 Conclusions and discussion

In this work, we have conducted a comprehensive investigation of a static, spherically symmetric black hole solution in scalar–tensor–vector gravity (STVG) surrounded by perfect fluid dark matter (PFDM). By incorporating both modified gravity and a phenomenological model for dark matter, we have systematically explored their combined impact on particle dynamics, thermodynamic stability, gravitational lensing, and black hole shadow formation. Our analysis of neutral and magnetized particle motion reveals that the presence of the MOG parameter α and the PFDM parameter λ significantly modifies the effective potential and the location of the innermost stable circular orbit (ISCO). We observe that increasing α tends to enhance orbital stability and shift the ISCO radius outward, while the PFDM component introduces additional modifications that strongly depend on the radial distribution of dark matter. From a thermodynamic perspective, we find that the Hawking temperature, entropy, and heat capacity are all altered by the presence of PFDM and MOG corrections. Notably, the black hole may undergo second-order

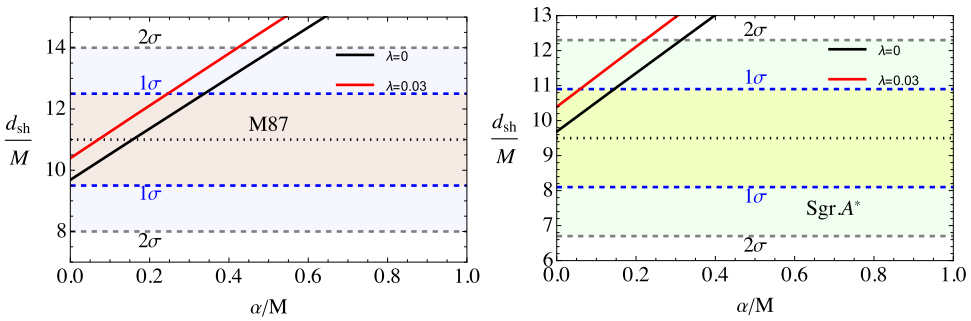

Fig. 16 Plot of the constraints for λ. The corresponding values of λ at the mean, 1σ, and 2σ confidence levels are shown

phase transitions, characterized by divergences in the heat capacity at critical horizon radii. The PFDM parameter λ is shown to raise the maximum Hawking temperature and shift the thermodynamic stability thresholds, while larger values of α suppress the temperature peak and alter the location of critical points. Our study of gravitational lensing, both in uniform and non-uniform plasma environments, indicates that the deflection angle is enhanced by PFDM and reduced by MOG effects. The bending of light rays is more pronounced in uniform plasma, with PFDM amplifying the lensing signal and α acting in the opposite direction. These results suggest that high-precision observations of lensed systems could help constrain the values of α and λ. We also explored the observable signature of black hole shadows and found that both α and λ led to an expansion in the shadow radius. The MOG parameter exerts a stronger influence, making it a key quantity in differentiating between general relativity and modified gravity scenarios. Comparing our theoretical shadow profiles with Event Horizon Telescope (EHT) data for M87* and Sgr A*, we constrained the parameter space of the model. Our results indicate that while GR remains consistent with current observations within the 1σ confidence interval, small deviations due to MOG and PFDM remain within the 2σ bounds and cannot be excluded. Overall, this study demonstrates that the interplay between modified gravity and fluid-like dark matter produces a rich phenomenology with potentially observable consequences. Future high-resolution black hole imaging and gravitational wave observations could further test the predictions of STVG+PFDM models and illuminate new aspects of gravity in the strong-field regime.

Acknowledgements The research is supported in part by grants FL-7923061954 of the Uzbekistan Ministry of Innovative Development.

Data availability statement This manuscript has no associated data. [Author's comment: Data sharing not applicable to this article as no datasets were generated or analysed during the current study].

Code Availability Statement This manuscript has no associated code/software. [Author's comment: Code/Software sharing not applicable to this article as no code/software was generated or analysed during the current study.].

Funded by SCOAP[3].

References

1. M.C. Miller, F.K. Lamb, Astrophys. J. Lett. **499**, L37 (1998). https://doi.org/10.1086/311335. arXiv:astro-ph/9711325 [astro-ph]
2. W. Kluźniak, Astrophys. J. Lett. **509**, L37 (1998). https://doi.org/10.1086/311748. arXiv:astro-ph/9712243 [astro-ph]
3. J.W. Moffat, J. Cosmol. Astropart. Phys. **2006**, 004 (2006). https://doi.org/10.1088/1475-7516/2006/03/004. arXiv:gr-qc/0506021 [gr-qc]
4. O.Y. Tsupko, G.S. Bisnovatyi-Kogan, Gravit. Cosmol. **15**, 184 (2009). https://doi.org/10.1134/S0202289309020182
5. M.A. Abramowicz, W. Kluźniak, Astron. Astrophys. **374**, L19 (2001). https://doi.org/10.1051/0004-6361:20010791. arXiv:astro-ph/0105077 [astro-ph]
6. I. Nishonov, J. Rayimbaev, S.U. Khan, M. Zahid, T. Tolibjanov, I. Ibragimov, Eur. Phys. J. C **85**, 325 (2025). https://doi.org/10.1140/epjc/s10052-025-13945-0
7. I. Nishonov, M. Zahid, S.U. Khan, J. Rayimbaev, A. Abdujabbarov, Eur. Phys. J. C **84**, 829 (2024). https://doi.org/10.1140/epjc/s10052-024-13204-8
8. J.W. Moffat, JCAP **03**, 004 (2006). https://doi.org/10.1088/1475-7516/2006/03/004. arXiv:gr-qc/0506021
9. S. Murodov, J. Rayimbaev, B. Ahmedov, A. Hakimov, Symmetry **15**, 2084 (2023). https://doi.org/10.3390/sym15112084. arXiv:2310.08046 [gr-qc]
10. S. Ullah Khan, J. Rayimbaev, Z. Stuchlík (2023). https://doi.org/10.48550/arXiv.2311.16936. arXiv:2311.16936 [gr-qc]
11. B. Turimov, J. Rayimbaev, A. Abdujabbarov, B. Ahmedov, Z. Stuchlík, Phys. Rev. D **102**, 064052 (2020). https://doi.org/10.1103/PhysRevD.102.064052. arXiv:2008.08613 [gr-qc]
12. S.U. Khan, J. Ren, Am. Inst. Phys. Conf. Ser. **2319**, 040005 (2021). https://doi.org/10.1063/5.0039635

13. S.U. Khan, U. Uktamov, J. Rayimbaev, A. Abdujabbarov, I. Ibragimov, Z.-M. Chen, Eur. Phys. J. C **84**, 203 (2024). https://doi.org/10.1140/epjc/s10052-024-12567-2
14. A. Abdujabbarov, A. Tursunov, B. Ahmedov, A. Kuvatov, Astrophys. Space Sci. **343**, 173 (2013)
15. J.W. Moffat, J. Cosmol. Astropart. Phys. **2024**, 079 (2024). https://doi.org/10.1088/1475-7516/2024/05/079. arXiv:2311.17130 [gr-qc]
16. C.-K. Qiao, M. Zhou, J. Cosmol. Astropart. Phys. **2023**, 005 (2023). https://doi.org/10.1088/1475-7516/2023/12/005. arXiv:2212.13311 [gr-qc]
17. F. Rahaman, K.K. Nandi, A. Bhadra, M. Kalam, K. Chakraborty, Phys. Lett. B **694**, 10 (2010). https://doi.org/10.1016/j.physletb.2010.09.038. arXiv:1009.3572 [gr-qc]
18. K. Haydarov, J. Rayimbaev, A. Abdujabbarov, S. Palvanov, D. Begmatova, Eur. Phys. J. C **80**, 399 (2020). https://doi.org/10.1140/epjc/s10052-020-7992-9. arXiv:2004.14868 [gr-qc]
19. S.U. Khan, M. Shahzadi, J. Ren, Phys. Dark Universe **26**, 100331 (2019). https://doi.org/10.1016/j.dark.2019.100331. arXiv:2005.09415 [gr-qc]
20. S. Kutlimuratov, N. Otojanova, I. Tadjibaev, K. Tillaboev, EUREKA Phys. Eng. **4**(2024), 3 (2024). https://doi.org/10.21303/2461-4262.2024.003416
21. G. Bertone, D. Hooper, J. Silk, Phys. Rep. **405**, 279 (2005). https://doi.org/10.1016/j.physrep.2004.08.031. arXiv:hep-ph/0404175 [hep-ph]
22. A. Das, A.R. Chowdhury, S. Gangopadhyay, Class. Quantum Gravity **41**, 015018 (2024). https://doi.org/10.1088/1361-6382/ad0fb7. arXiv:2306.00646 [gr-qc]
23. J.R. Mureika, J.W. Moffat, M. Faizal, Phys. Lett. B **757**, 528 (2016). https://doi.org/10.1016/j.physletb.2016.04.041. arXiv:1504.08226 [gr-qc]
24. A. Das, A. Saha, S. Gangopadhyay (2020). https://doi.org/10.48550/arXiv.2009.03644. arXiv:2009.03644 [gr-qc]
25. I.D. Novikov, K.S. Thorne, in *Black Holes (Les Astres Occlus)*, pp. 343–450 (1973)
26. W.-H. Bian, Y.-H. Zhao, Publ. Astron. Soc. Jpn. **55**, 599 (2003). https://doi.org/10.1093/pasj/55.3.599. arXiv:astro-ph/0305095 [astro-ph]
27. S. Mahapatra, I. Banerjee, Phys. Dark Univ. **39**, 101172 (2023). https://doi.org/10.1016/j.dark.2023.101172. arXiv:2208.05796 [gr-qc]
28. G.S. Bisnovatyi-Kogan, O.Y. Tsupko, Mon. Not. R. Astron. Soc. **404**, 1790 (2010). https://doi.org/10.1111/j.1365-2966.2010.16290.x. arXiv:1006.2321 [astro-ph.CO]
29. F. Atamurotov, I. Hussain, G. Mustafa, A. Övgün, Chin. Phys. C **47**, 025102 (2023). https://doi.org/10.1088/1674-1137/ac9fbb
30. T. Ibrokhimov, Z. Turakhonov, F. Atamurotov, A. Abdujabbarov, K. Yerzhanov, G. Bauyrzhan, A. Abduvokhidov, Phys. Dark Univ. **47**, 101778 (2025). https://doi.org/10.1016/j.dark.2024.101778
31. A. Alimova, Z. Turakhonov, F. Atamurotov, A. Abdujabbarov, Phys. Dark Univ. **47**, 101749 (2025). https://doi.org/10.1016/j.dark.2024.101749
32. Z. Turakhonov, F. Atamurotov, A. Övgün, A. Abdujabbarov, S. Urinov, Commun. Theor. Phys. **76**, 115401 (2024). https://doi.org/10.1088/1572-9494/ad6853
33. Z. Turakhonov, F. Atamurotov, S.G. Ghosh, A. Abdujabbarov, Phys. Dark Univ. **48**, 101880 (2025). https://doi.org/10.1016/j.dark.2025.101880
34. V. Perlick, O.Y. Tsupko, Phys. Rep. **947**, 1 (2022). https://doi.org/10.1016/j.physrep.2021.10.004. arXiv:2105.07101 [gr-qc]
35. V. Perlick, O.Y. Tsupko, G.S. Bisnovatyi-Kogan, Phys. Rev. D **92**, 104031 (2015). https://doi.org/10.1103/PhysRevD.92.104031. arXiv:1507.04217 [gr-qc]
36. K. Karshiboev, F. Atamurotov, A. Abdujabbarov, A. Övgün, A. Reyimberganov, Commun. Theor. Phys. **76**, 025401 (2024). https://doi.org/10.1088/1572-9494/ad1583
37. B. Rahmatov, M. Zahid, S.U. Khan, J. Rayimbaev, I. Ibragimov, Z. Yuldoshev, A. Dauletov, S. Muminov, Chin. Phys. C **49**, 075105 (2025). https://doi.org/10.1088/1674-1137/adc188
38. M. Zhang, M. Guo, Eur. Phys. J. C **80**, 790 (2020). https://doi.org/10.1140/epjc/s10052-020-8389-5. arXiv:1909.07033 [gr-qc]
39. S.-B. Yuan, C.-K. Luo, Z.-Z. Hu, Z.-Y. Zhang, B. Chen, Chin. Phys. C **49**, 025103 (2025). https://doi.org/10.1088/1674-1137/ad9148. arXiv:2403.06886 [gr-qc]
40. A. Abdujabbarov, M. Amir, B. Ahmedov, S.G. Ghosh, Phys. Rev. D **93**, 104004 (2016). https://doi.org/10.1103/PhysRevD.93.104004. arXiv:1604.03809 [gr-qc]
41. F. Atamurotov, U. Papnoi, K. Jusufi, Class. Quantum Gravity **39**, 025014 (2022). https://doi.org/10.1088/1361-6382/ac3e76. arXiv:2104.14898 [gr-qc]
42. Z. Zhong, Z. Hu, H. Yan, M. Guo, B. Chen, Phys. Rev. D **104**, 104028 (2021). https://doi.org/10.1103/PhysRevD.104.104028. arXiv:2108.06140 [gr-qc]
43. Z. Hu, Z. Zhong, P.-C. Li, M. Guo, B. Chen, Phys. Rev. D **103**, 044057 (2021). https://doi.org/10.1103/PhysRevD.103.044057. arXiv:2012.07022 [gr-qc]
44. K. Akiyama et al. [Event Horizon Telescope], Astrophys. J. Lett. **930**, L12 (2022). https://doi.org/10.3847/2041-8213/ac6674. arXiv:2311.08680 [astro-ph.HE]
45. K. Akiyama et al., ApJ **875**, L1 (2019). https://doi.org/10.3847/2041-8213/ab0ec7. arXiv:1906.11238 [astro-ph.GA]